

# Physical effects of mechanical design parameters on photon sensitivity and spatial resolution performance of a breast-dedicated PET system

V. C. Spanoudaki, F. W. Y. Lau, A. Vandenbroucke, and C. S. Levin<sup>a)</sup>

*Department of Radiology and the Molecular Imaging Program at Stanford, Stanford University, Stanford, California 94305-5128*

(Received 28 March 2010; revised 30 June 2010; accepted for publication 27 July 2010; published 19 October 2010)

**Purpose:** This study aims to address design considerations of a high resolution, high sensitivity positron emission tomography scanner dedicated to breast imaging.

**Methods:** The methodology uses a detailed Monte Carlo model of the system structures to obtain a quantitative evaluation of several performance parameters. Special focus was given to the effect of dense mechanical structures designed to provide mechanical robustness and thermal regulation to the minuscule and temperature sensitive detectors.

**Results:** For the energies of interest around the photopeak (450–700 keV energy window), the simulation results predict a 6.5% reduction in the single photon detection efficiency and a 12.5% reduction in the coincidence photon detection efficiency in the case that the mechanical structures are interspersed between the detectors. However for lower energies, a substantial increase in the number of detected events (approximately 14% and 7% for singles at a 100–200 keV energy window and coincidences at a lower energy threshold of 100 keV, respectively) was observed with the presence of these structures due to backscatter. The number of photon events that involve multiple interactions in various crystal elements is also affected by the presence of the structures. For photon events involving multiple interactions among various crystal elements, the coincidence photon sensitivity is reduced by as much as 20% for a point source at the center of the field of view. There is no observable effect on the intrinsic and the reconstructed spatial resolution and spatial resolution uniformity.

**Conclusions:** Mechanical structures can have a considerable effect on system sensitivity, especially for systems processing multi-interaction photon events. This effect, however, does not impact the spatial resolution. Various mechanical structure designs are currently under evaluation in order to achieve optimum trade-off between temperature stability, accurate detector positioning, and minimum influence on system performance. © 2010 American Association of Physicists in Medicine. [DOI: 10.1118/1.3484059]

Key words: positron emission tomography (PET), high resolution, breast imaging, Monte Carlo simulations, photon sensitivity, spatial resolution

## I. INTRODUCTION

Recent developments in technology have lead to advanced imaging systems and methods for accurately detecting and monitoring breast cancer using imaging modalities that complement information provided by mammography.<sup>1,2</sup> Positron emission tomography (PET) demonstrates great potential in this regard due to the high cancer avidity of PET imaging agents, as well the ability to enable *in vivo* imaging of the underlying cellular and molecular biology of breast cancer.<sup>3,4</sup> However, special considerations on detector design and system architecture need to be taken into account given the demands for high spatial resolution and high photon sensitivity in order to detect early stages of breast cancer, which cannot be satisfied with the current clinical tomograph designs.<sup>5–9</sup> Breast-dedicated PET systems have recently demonstrated their clinical relevance,<sup>10</sup> whereas specialized system designs may be used to improve system performance.<sup>11</sup>

Our group is developing a 1 mm<sup>3</sup> resolution PET scanner dedicated to breast imaging.<sup>12</sup> The system will be composed of a large number of compact detector modules, each comprising 8 × 8 arrays of 1 mm<sup>3</sup> lutetium yttrium oxyorthosilicate (LYSO) scintillation crystals optically coupled to position sensitive avalanche photodiodes (PSAPDs).<sup>13,14</sup> Two opposing detector panels will be assembled, thus allowing for limited-angle tomographic imaging (Fig. 1) if rotation is not employed. The adjustable separation between the two panel detectors will lead to a tenfold increased photon sensitivity compared to clinical PET scanners.<sup>12</sup> In addition, photon sensitivity is maintained through an effective crystal length of nearly 1.6 cm by using two crystal arrays oriented along the radial direction (“edge on” photon detection, as illustrated in Fig. 2). Also, in this scintillation detection configuration, the scintillation light collection efficiency is >90%, independent of the photon interaction location in the system.<sup>14</sup> Furthermore, this design enables fine (~1 mm) photon depth of interaction (DoI) information, which enables

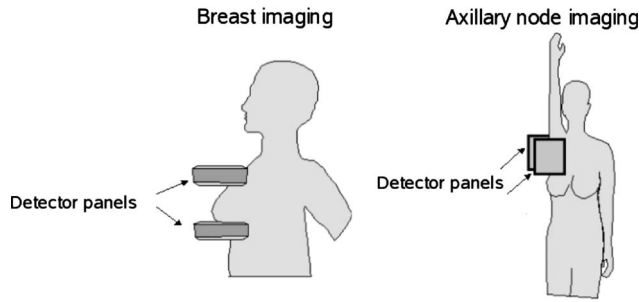


FIG. 1. Two different orientations of the dual-panel breast PET imaging system, for breast and axillary node imaging, currently under development.

a high degree of spatial resolution uniformity throughout the sensitive volume of the field of view (FoV). At the same time, detectors employing this type of DoI architecture are able to identify the 3D coordinates of every photon interaction rather than just the centroid of multiple interactions that is available to alternative DoI architectures.<sup>15,16</sup> In such dense detector design, elimination of sources of uncertainty that hinder the reproducibility of various system operation parameters assures reliable performance. Such sources of uncertainty are temperature variations in the detector vicinity, which may lead to detector gain drifts and therefore affect system calibration,<sup>17</sup> as well as detector positioning errors, which may lead to artifacts in the reconstructed image and thus affect image quality. In order to ensure accurate positioning of the minute detector elements, the design employs special mechanical structures. These structures will also provide thermal regulation of the temperature sensitive semicon-

ductor photodetectors. However, the presence of additional material interspersed between crystals (Fig. 3) may cause attenuation or scatter of the annihilation photons, thus influencing both the detection efficiency and the accuracy to which coincidence events are localized.

In addition, photons that have scattered among different detector elements (multi-interaction photon events, henceforth referred to as MIPES) may be affected by the presence of additional material interspersed between the crystals. It should be noted that in the system under study, MIPES are identified solely for photons depositing energy in different  $8 \times 8$  LYSO-PSAPD arrays. Due to the inherent charge multiplexing with the PSAPD's resistive sheet, MIPES among crystal elements of the same  $8 \times 8$  array cannot be individually localized. Instead, the energy sum of all the involved interactions of a single photon within a crystal array is recorded and the detector places the event at their centroid within a single PSAPD. The simulation described in the following processes those intra-array events in a similar manner.

It will be shown that the mechanical structures act as an additional scattering medium for the incident annihilation photons. This results in substantial degradation of detection efficiency because of the resulting change in scattering angle, which may lead to either the detection of the scattered photon by a different detector element or to the complete removal in the case that the photon is photoabsorbed in the material or scattered outside the FoV. Our system design aims to take into account such multi-interaction photon events by using appropriate positioning algorithms<sup>18,19</sup> in or-

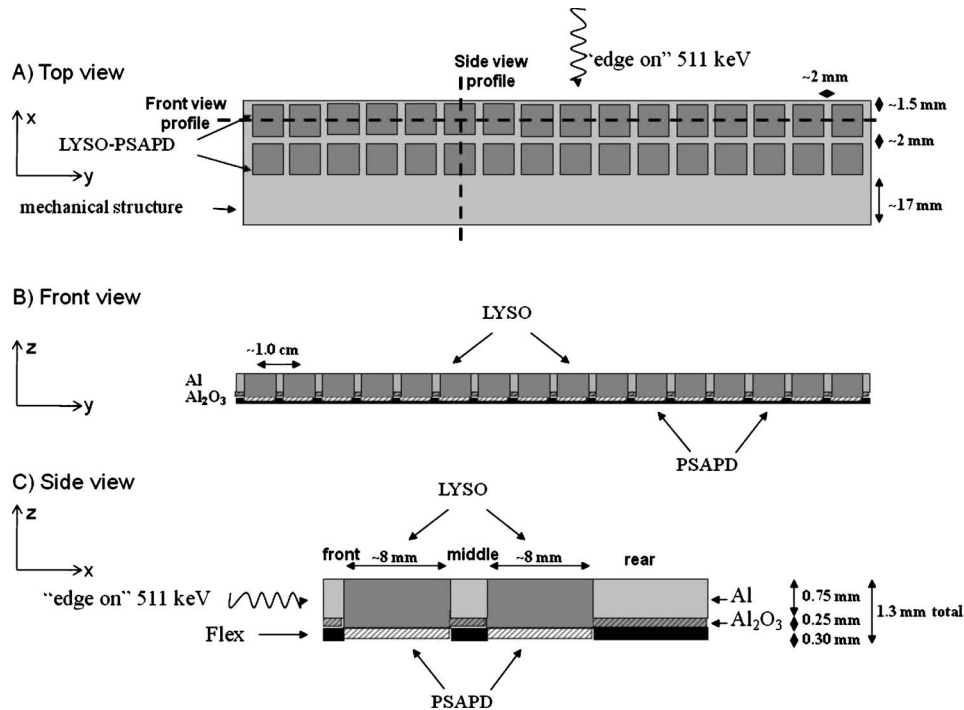


FIG. 2. Top (a), front (b), and side (c) views of the LYSO-PSAPD modules with the mechanical structures (Al and  $\text{Al}_2\text{O}_3$ ) interspersed. Also shown is the position of the PSAPDs with respect to the LYSO crystals, as well as the flex circuits used to bias the PSAPDs and connect their signals to the subsequent processing electronics. The axes definition for each view is shown in the figure.

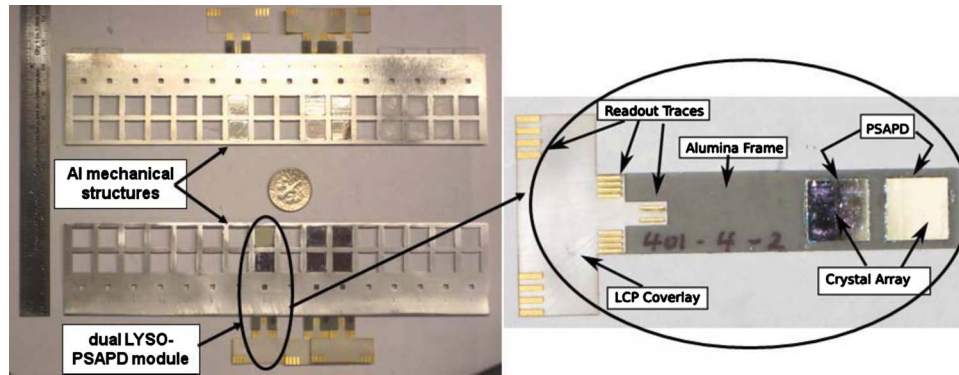


Fig. 3. Left: Photo of the Al structures used to provide mechanical alignment and thermal regulation for 16 detector modules. Right: Photo of a dual LYSO-PSAPD detector module used in the system.

der to enhance photon sensitivity without degrading spatial resolution, as studies from other groups have already demonstrated.<sup>20,21</sup>

The purpose of this work is to investigate the effect of these structures on specific aspects of the tomograph's performance, primarily in terms of photon sensitivity and spatial resolution. The results have relevant implications for understanding the potential effects that mechanical structures in PET system designs can have on the performance. These implications become more important in modern designs given their increased complexity dictated by the requirement for high resolution, quantitative imaging. Proper mechanical design plays a key role for the reliable operation of such high resolution PET systems and this study concludes this by using the paradigm of a high resolution breast-dedicated PET system.

## II. MATERIALS AND METHODS

### II.A. System design and model

Each detector module consists of two (a front and rear)  $8 \times 8$  LYSO crystal arrays mounted on two PSAPDs [each array consists of  $1 \times 1 \times 1$  mm<sup>3</sup> crystal elements with a pitch of 1 mm in both  $x$  and  $y$  directions, Fig. 3 (right)]. The two detectors are physically connected to each other through a common flex circuit that is used to bias the detectors and connect the detector signals to the subsequent processing electronics. An Al<sub>2</sub>O<sub>3</sub> frame provides mechanical support of the module as well as enables accurate positioning of the front detector array with respect to the rear one.<sup>22</sup> The complete dual layer detector module (LYSO arrays, PSAPDs, and alumina frame) is shown in Fig. 3 (right). In addition, an Al fin is used to provide heat dissipation as well as accurate relative positioning between neighboring dual layer detector modules and includes openings to accommodate 16 such modules, as shown in Fig. 3 (left). A side view of a LYSO-PSAPD module with the Al and Al<sub>2</sub>O<sub>3</sub> structures interspersed is shown in Fig. 2(c). The total thickness of the detector module is 1.3 mm, of which  $\sim 300$   $\mu$ m is the thickness of the PSAPDs plus the flex circuit used to bias the PSAPDs and read out their signals on each module. The residual 1 mm is the thickness of the crystal arrays (includ-

ing 70  $\mu$ m of reflector polymer on top of each array) as well as of the Al plus Al<sub>2</sub>O<sub>3</sub> structures enclosing them (see Fig. 2). The thickness of the Al structures is critical since it should be adequately large for efficient thermal dissipation but also as small as possible for minimal sensitivity losses.

In total, 144 of these Al fin structures (72 of which comprising one detector panel shown in Fig. 1) will be used in the complete system to provide mechanical alignment and thermal regulation for 4608 LYSO-PSAPD detector arrays. An overview of the infrastructure of a detector panel is shown in Fig. 4.

The following analysis is based on simulation results created with the GRAY ray tracing simulation package developed in our group.<sup>23</sup> Two 3.7 MBq radioactive water configurations, one confined to a small (10  $\mu$ m diameter) sphere and the other in a uniform 3.5 cm thick slab placed between the two panels to simulate compressed breast tissue, were simulated for each of the two different tomograph configurations:

- The first "ideal" simulated configuration includes no mechanical structures, in place of which air is assumed between detectors.
- The second configuration includes a mechanical structure comprising a sheet of Al and an Al<sub>2</sub>O<sub>3</sub> frame supporting the LYSO-PSAPD detector modules with an overall 1 mm thickness embedded around the crystals (the Al structure has a thickness of 750  $\mu$ m and the Al<sub>2</sub>O<sub>3</sub> frame has a thickness of 250  $\mu$ m) (see Fig. 2).

In order to fully exploit the fast processing speed of the GRAY code, in each of the above configurations the crystal arrays are actually modeled as crystal slabs and subsequently the software analysis considers the LYSO crystal array pixelation ( $8 \times 8$ ) by segmenting the resulting interactions into an  $8 \times 8$  matrix of  $1 \times 1 \times 1$  mm<sup>3</sup> bins. Figure 5 illustrates the simulated arrangement of the detector arrays in the two opposing detector panels, as well as that of the mechanical structures. Also shown in the images are the two simulated sources and their topology with respect to the detector panels. The points forming dark colored squares represent simulated interactions occurring in the actual LYSO arrays. All the other points (forming light colored structures) represent

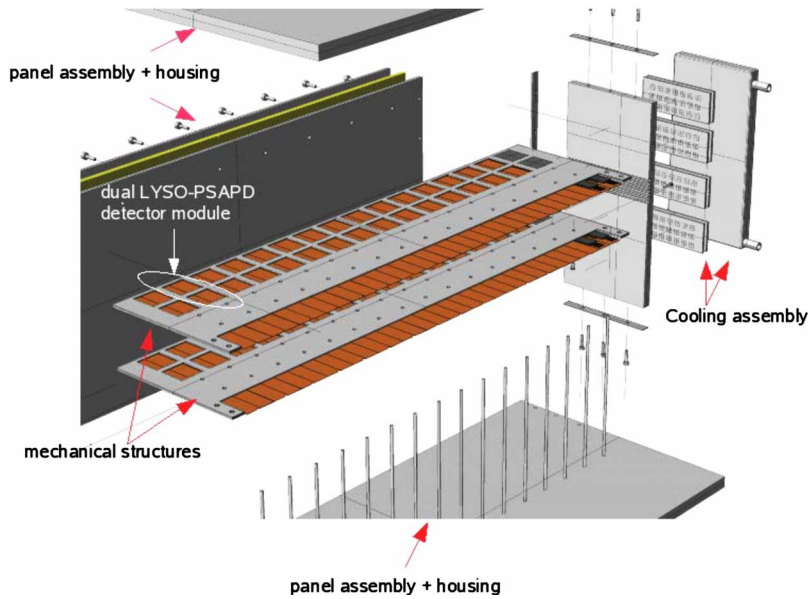


FIG. 4. Overview of the infrastructure of a detector panel: 2 out of 72 Al mechanical structures of one detector panel are shown in the figure. Each mechanical structure accommodates 16 dual LYSO-PSAPD detector modules (one dual module is designated with the white ellipse in figure). The cooling and housing assembly is also shown in the figure. A complete detector panel will measure approximately  $20 \times 12 \times 8$  cm<sup>3</sup>.

simulated photon interactions occurring in a nondetector material such as the source and the mechanical structures.

In a separate simulation study, the effect of the PSAPD material alone was investigated by introducing an additional Si layer with a thickness of 0.3 mm in between the axial crystal layers, as illustrated in Fig. 2(c). It should be noted that only in this specific simulation was the PSAPD material included (otherwise replaced by air), in an effort to monitor the effect of the mechanical structures alone as the sole nondetector material apart from the LYSO crystal arrays. For all the simulations presented in this study, the GRAY package does not consider the effect of positron range.

### II.B. Photon sensitivity: Singles, coincidence, and multi-interaction photon events

At first, this study estimates the effect of the additional material between the detectors on the number of the detected single photons (singles events) as well as on the number of registered coincidences for various energy windows, for the

two different source configurations described above. Gaussian blurring was introduced to the registered energy and time stamp of every detected singles event in order to model detector elements which have an energy resolution of 15% at 511 keV and a pair coincidence time resolution of 5 ns (FWHM). These values are chosen to be on the high end of the deviation of the reported measured average values.<sup>24</sup> The analysis identifies coincidence events from the recorded singles events by choosing a 10 ns wide timing window that scans the singles list-mode data stream after the detected events have been sorted in time. The study considered coincidences between two detectors from opposing panels forming a physically meaningful line of response, as well as coincidences between detectors belonging to the same panel involved in MIPES (defined above).

In the case of MIPES (both between different arrays as well as within the same array), the energy threshold was set with respect to the sum of the energies deposited for all interactions of a single photon occurring anywhere in one

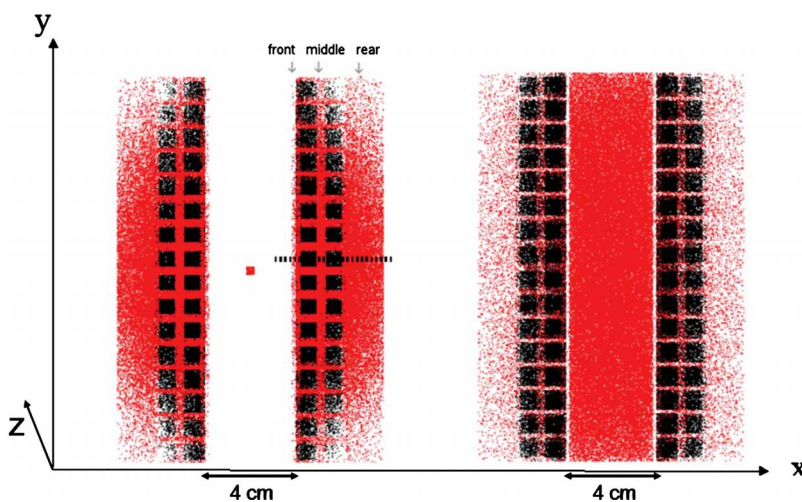


FIG. 5. Interaction histogram of the simulated scanner configuration (interactions from all 72 layers of each detector panel are summed) with a point source (left) and a uniform slab source (right) placed at the center of the FoV. The axial extent ( $z$ ) of the tomograph is not shown in the image. The points forming dark colored squares represent photon interactions in the LYSO detectors and all the other points (forming light colored structures) represent interactions in a nondetector material such as the source between the panels and the embedded Al and Al<sub>2</sub>O<sub>3</sub> mechanical structures in the panels.

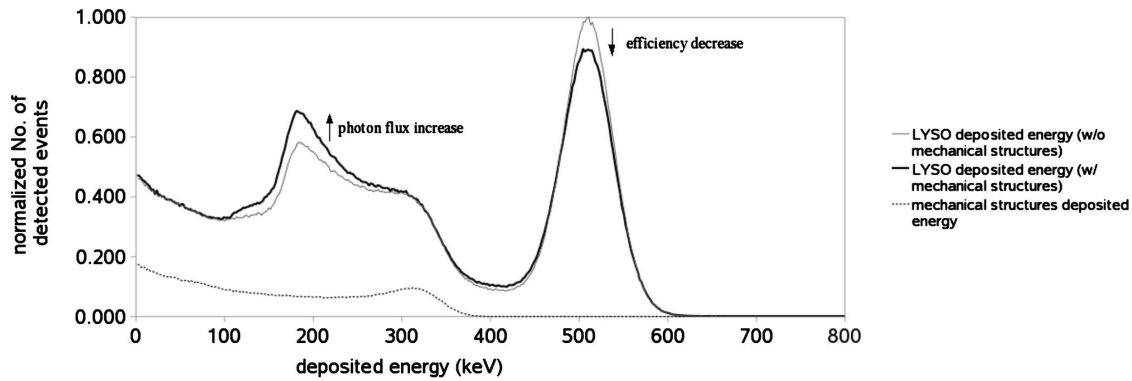


FIG. 6. Comparative spectra of deposited energy of singles events in LYSO in the simulated case of no mechanical structures interspersed between the detectors (gray line) and in the case of mechanical structures interspersed (black line). A histogram of the energy deposited in the mechanical structures is also shown (dashed black line).

panel. For the current analysis, and due to the different focus of this study, no correction for accidental coincidences was performed, given the low random background observed on the coincidence time histograms for the source activities employed in this study (3.7 MBq for both point and uniform sources). The effect of the mechanical structures on the number of MIPes was also studied.

### II.C. Spatial resolution: Intrinsic and reconstructed

In order to estimate how the spatial resolution would be affected by the presence of mechanical structures, the simulation steps a point source along the axial and transaxial directions spanning one complete  $8 \times 8$  crystal array (with all 72 layers of each detector panel present). The number of detected coincidences belonging to the same projection view parallel to a line connecting the two detector panels and passing through the source was plotted as a function of source position. The step size was chosen to be  $125 \mu\text{m}$ , namely,  $\frac{1}{8}$  of the crystal pixel size along the axial and transaxial directions. In addition, images of point sources placed at different radial offsets from the center of the FoV were reconstructed using the ordered subset expectation maximization (OSEM) algorithm and the dependence of the FWHM of the corresponding profiles on radial offset was estimated for four different cases:

- (1) System configuration with mechanical structures; MIPes are included in the reconstruction.
- (2) System configuration without mechanical structures; MIPes are included in the reconstruction.
- (3) System configuration with mechanical structures; MIPes are not included in the reconstruction.
- (4) System configuration without mechanical structures; MIPes are not included in the reconstruction.

For all the above simulation cases, the acquisition time was identical (1 s) in order to assess how the reduced sensitivity in the case of interspersed mechanical structures would affect the spatial resolution of the system.

## III. RESULTS

### III.A. Photon sensitivity: Singles, coincidence, and multi-interaction photon events

#### III.A.1. Energy deposited from single photons

Figure 6 shows histograms of the deposited energy in both the crystal and the mechanical structure material from photons (emitted from a point source) that have deposited either a part of their energy via the Compton scatter interaction process or the full amount of their energy via photoelectric absorption. The accepted event energies lie within the 0–700 keV window. It should be noted that a blurring component equal to the simulated energy resolution of the LYSO-PSAPD detectors was also added to the energy deposited in the mechanical structures in order to facilitate visual correlation to the energy deposition in LYSO.

#### III.A.2. Spatial information of singles events

In order to better understand how the specific geometry of the mechanical structures affects sensitivity, this study considers interaction profiles along the  $x$  and  $z$  directions, as designated in Fig. 5, and investigates their features, as shown in Fig. 7. The left plot shows an  $x$  profile through the middle of a single LYSO-PSAPD detector module where both active detector elements and parts of the 1 mm thick

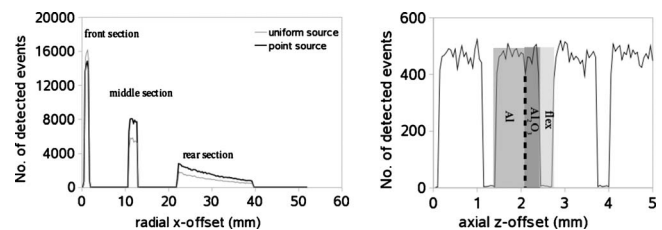


FIG. 7. Simulated interaction profiles along the  $x$  axis, as illustrated in Fig. 5 with the dashed line (left), as well as along the  $z$  axis (right). The different sections of the mechanical structure (indicated as front, middle, and rear) are also shown in Fig. 5. The highlighted regions on the  $z$  profile (for one detector layer) indicate the  $750 \mu\text{m}$  thick Al layer (gray), the  $250 \mu\text{m}$   $\text{Al}_2\text{O}_3$  layer (dark gray), and the  $300 \mu\text{m}$  flex circuit (light gray).

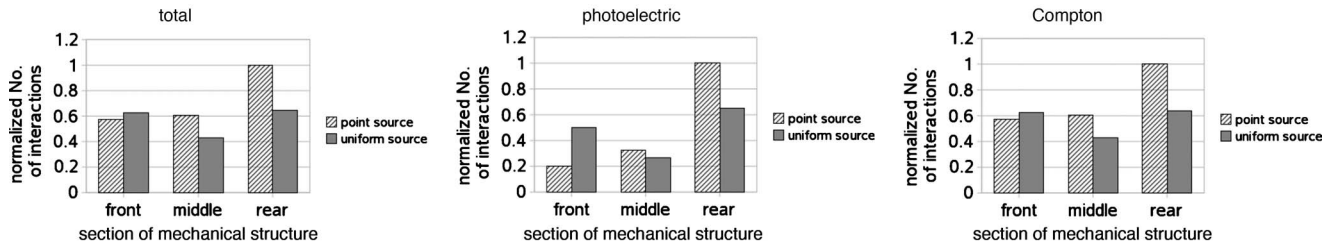


Fig. 8. Comparative bar diagram of total (left), photoelectric (middle), and Compton (right) interactions (normalized to the maximum recorded number) occurring in the front, middle, and rear sections of the mechanical structures (based on Fig. 7) for a point and a uniform source (as designated in Fig. 5).

Al<sub>2</sub>O<sub>3</sub> support+Al fin layer structures are present (the profile is illustrated with a dashed line in Fig. 5). In order to enhance statistical accuracy, the profile is integrated over the complete *z* and *y* extent of the detector panel (all interactions over all layers in one detector panel that occur in the same position range across each dual module are projected onto a single line along the *x* direction). The right plot shows a *z* profile integrated over the complete *x*- and *y* extent of the detector panel (all interactions over all layers in one detector panel that occur in the same position range across each dual module are projected onto a single line along the *z* direction). The *z* profile is given in the figure for the case of the uniform source in order to avoid patterns such as sensitivity variations due to limited source coverage of the detector. It should be noted that the incident photon events considered in Fig. 7 may have a wide range of energies other than 511 keV, depending on whether they have suffered scatter in the source material (an effect mostly prominent for the uniform compared to the point source). Therefore, photoelectric absorption may occur for energies lower than 511 keV. Figure 8 illustrates quantitatively the total number of interactions in

each section. The relative number of photoelectric and Compton interactions for each section are also shown in separate graphs in the figure.

**III.A.3. Energy and spatial correlation of detection efficiency**

Figure 9 shows histograms of the energy deposited in the mechanical structures for the three parts designated in Figs. 2, 5, and 7. As opposed to Fig. 8, in these histograms there is no distinction between different interaction types, namely, both Compton scatter and photoelectric absorption are included. As previously mentioned, the vast majority of interactions on the mechanical structures will be Compton scatter. A photopeak at 511 keV is not visible in either spectrum because of the extremely weak probability of full energy deposition of a high energetic quantum (511 keV) at the material of the mechanical structures. However, photoelectric absorption still occurs for lower energetic (previously scattered) quanta, as verified in the graphs of Fig. 8.

Figure 10 shows the relative reduction in the number of detected single and coincidence photon events in the scintillation crystals defined as

$$\text{change in detection efficiency} = \frac{\text{No. of detected events}_{w/o \text{ mech. struct.}} - \text{No. of detected events}_{w. \text{ mech. struct.}}}{\text{No. of detected events}_{w/o \text{ mech. struct.}}} \cdot 100\% \quad (1)$$

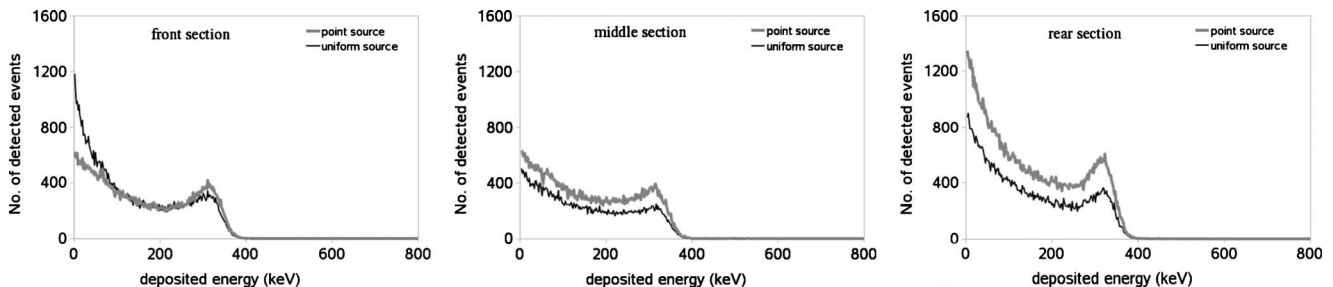


Fig. 9. Histograms of the energy deposited in the front, middle, and rear sections of the mechanical structures designated in Figs. 2, 5, and 7 for a point source (gray) and for a uniform source (black).

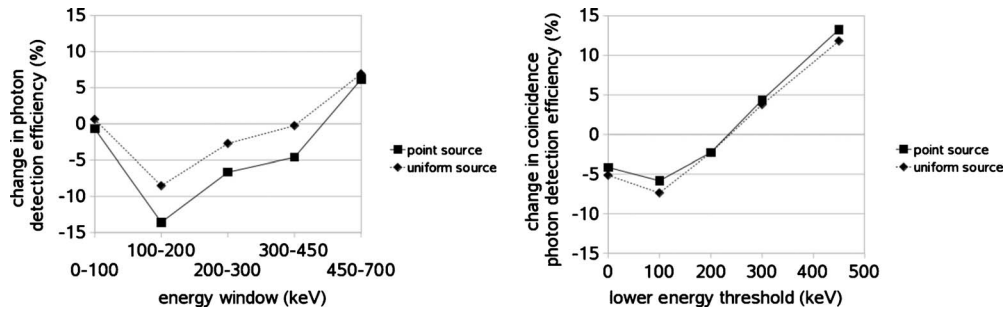


FIG. 10. Relative change in singles (left) and coincidence (right) detection efficiency with and without the structures present for a point source (squares) and a uniform source (diamonds). The change in detection efficiency is plotted as a function of different energy windows, which in the case of singles have variable lower and upper limits and in the case of coincidences have a fixed upper limit at 700 keV and a variable lower limit.

for the two panel configurations with and without interspersed mechanical structures present, for two different source geometries (point and uniform slab), and for various energy windows. For the energy window of 450–700 keV, which is of primary interest in PET, a reduction of 6.5% and approximately 12.5% in the singles and coincidence events is observed due to the presence of the mechanical structures. Additional simulations show that 25% of the abovementioned reduction is attributed to the 250  $\mu\text{m}$  thick  $\text{Al}_2\text{O}_3$  layer and 75% is attributed to the 750  $\mu\text{m}$  thick Al layer, thus scaling in a linear manner with the material thickness and not being dependent on the different densities of Al and  $\text{Al}_2\text{O}_3$  (2.7 and 3.7  $\text{g}/\text{cm}^3$ , respectively), as also shown from the right graph (interaction profile along the  $z$  direction) of Fig. 7. A chart comparing the relative singles and coincidence event reduction between any two of the following three cases is shown in Fig. 11:

- System with no mechanical structures interspersed within LYSO-PSAPD detectors;
- System with only a 250  $\mu\text{m}$  thick  $\text{Al}_2\text{O}_3$  layer interspersed within the detectors; and
- System with a 250  $\mu\text{m}$  thick  $\text{Al}_2\text{O}_3$  layer and a 750  $\mu\text{m}$  thick Al layer interspersed.

The analysis considers the intermediate second case (system with only a 250  $\mu\text{m}$  thick  $\text{Al}_2\text{O}_3$  layer interspersed

within the detectors) given the fact that the  $\text{Al}_2\text{O}_3$  frame (Fig. 3, right) appears as an inherent component of the front-end construction. The Al fin (Fig. 3, left) is the actual mechanical structure additionally manufactured and thus the one whose dimensions would have to be adjusted in case of significant performance degradation predicted by the simulations. The additional simulations shown in Fig. 11 were performed for the same energy window of 450–700 keV and the mean values of efficiency reduction between point and uniform source are shown.

The study also considered the effect of the PSAPD material (Si) even though the photodetectors are an inherent component of the 511 keV photon detection process, and thus no regulation of their dimensions is possible. The PSAPD material causes mean degradations of 2.1% and 4.2% for single photon and coincidence photon detection, respectively, for both source geometries (point and uniform).

#### III.A.4. Multi-interaction photon events

The number of MIPes is also expected to be affected by the presence of additional material interspersed between the LYSO-PSAPD detectors. In this study, MIPes have been identified during the coincidence sorting process from the list-mode data stream. MIPes are detected in the case that more than two total interactions for both coincidence pho-

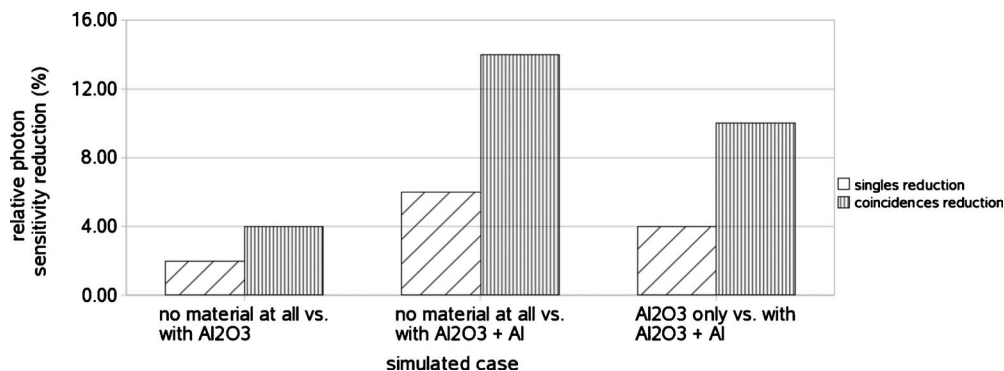


FIG. 11. Comparative chart of the relative photon sensitivity reduction (for both singles and coincidence events) for three different simulated cases: (i) A system with only a 250  $\mu\text{m}$  thick  $\text{Al}_2\text{O}_3$  layer compared to a system with no interspersed mechanical structures (“material”) at all, (ii) a system with a 250  $\mu\text{m}$  thick  $\text{Al}_2\text{O}_3$  layer and a 750  $\mu\text{m}$  thick Al layer compared to a system with no material at all, and (iii) a system with a 250  $\mu\text{m}$  thick  $\text{Al}_2\text{O}_3$  layer and a 750  $\mu\text{m}$  thick Al layer compared to a system with only a 250  $\mu\text{m}$  thick  $\text{Al}_2\text{O}_3$  layer. The results are calculated for a 450–700 keV energy window for both the point and uniform sources.

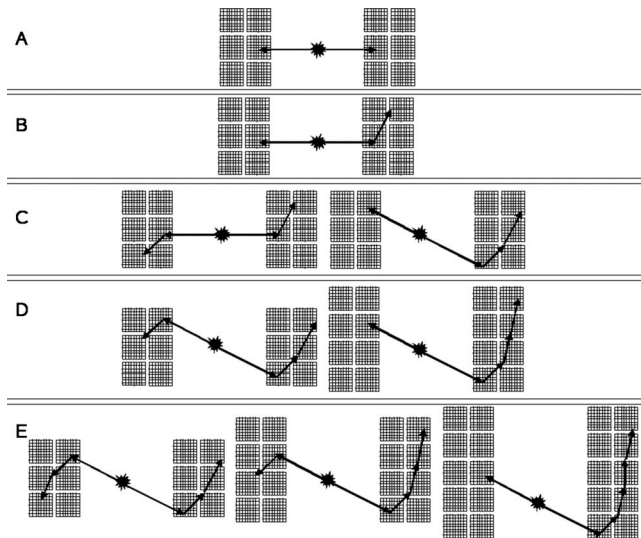


FIG. 12. Examples of two (a), three (b), four (c), five (d), and six (e) total interactions for two coincidence photons. The hatched structures represent the two  $8 \times 8$  LYSO arrays of the dual LYSO-PSAPD module. As previously mentioned, MIPES occurring within a single array cannot be identified as separate. The illustrated cases are symmetric to either detector side.

tions occur within the same time coincidence window and if these interactions satisfy specific geometrical conditions, that is, at least two interactions occurred at opposing panels. Some examples of these geometrical constraints are illustrated in Fig. 12 [cases (b)–(e)]. Table I shows quantitatively the relative decrease in coincidence events involving both single-interaction events and MIPES with and without the mechanical structures present. For the current study, only MIPES containing up to six total interactions for both coincidence photons within the same coincidence time window are considered. Figure 13 shows histograms of the total number of interactions for two coincident photon events for the case of a point and a uniform source.

### III.B. Spatial resolution: Intrinsic and reconstructed

#### III.B.1. Intrinsic spatial resolution

Figure 14 shows the coincidence detection profiles for a point source stepped for a total distance of 1 cm along different directions within the system's FoV. The transaxial profiles shown in Fig. 14 (bottom) have an overall width slightly

TABLE I. Relative reduction in coincidence events with and without the interspersed mechanical structures for the different cases illustrated in Fig. 12 based on the results shown in Fig. 13.

Total number of crystal interactions for both coincidence photons	Reduction (%)	
	Point source	Uniform source
2	11	10
3	13	12
4	16	15
5	18	11
6	21	11

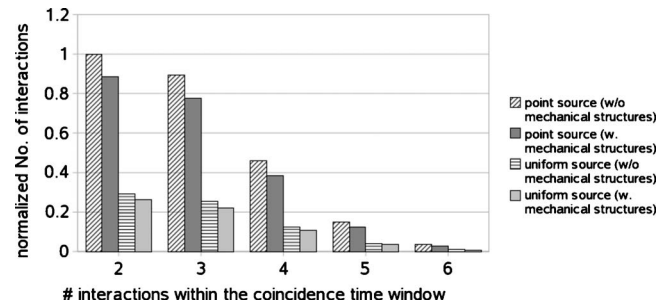


FIG. 13. The total number of interactions (normalized to the maximum number) for coincidence events in the two panels (see Fig. 12). The plot shows the simulated data for a point and a uniform source and for an energy window of 450–700 keV imposed at the energy sum of MIPES.

over 8 mm, which reflects the  $8 \times 8$  crystal array size. The fact that the crystal array has a physical transaxial offset of about 1 mm with respect to the center of the FoV (Fig. 5) results in a similar offset in the transaxial profiles.

In these profiles the various peaks correspond to the transaxial position of the crystal elements and the difference between two subsequent peaks corresponds to the crystal element pitch ( $\sim 1$  mm) within the  $8 \times 8$  array. In the axial direction the crystal array has only 1 mm thickness and this is the direction along which the mechanical structures are assumed to be stacked in order to form each detector panel. Each peak in the profiles of Fig. 14 (top) corresponds to the position of each axial layer and the difference between two subsequent peaks corresponds to the axial layer pitch ( $\sim 1.3$  mm) within each detector panel [Fig. 2(c)].

The crystal pitches of 1.3 and 1 mm along the axial ( $z$ ) and transaxial ( $y$ ) directions, respectively, can be easily observed by the plots of Fig. 14, with and without the structures present, from the distance between the centroids of neighboring profiles. Table II shows the calculated mean values over all neighboring profiles. The calculated crystal pitch values have the same number of significant digits as the step size of the point source ( $0.125 \mu\text{m}$ ) and the calculated standard deviation is equal to approximately half the stepping accuracy.

The calculated mean FWHM value of the axial (along  $z$ ) and transaxial profiles (along  $y$ ) over all source positions is shown in Table III for the case of no material and for the case of mechanical structures ( $\text{Al}_2\text{O}_3 + \text{Al}$ ) present, respectively. In the case of MIPES, although other event identification methods are under investigation,<sup>18,19</sup> in this work, positioning of the event is based on the energy weighted mean coordinates of all the interactions per photon, as described by Eq. (2),

$$x_{\text{mean}} = \frac{\sum E_i x_i}{\sum E_i}, \quad y_{\text{mean}} = \frac{\sum E_i y_i}{\sum E_i}, \quad z_{\text{mean}} = \frac{\sum E_i z_i}{\sum E_i}, \quad (2)$$

where  $E_i$  is the energy deposited during the  $i$ th interaction, and  $x_i$ ,  $y_i$ , and  $z_i$  are the  $x$ ,  $y$ , and  $z$  coordinates of the  $i$ th interaction point, respectively.

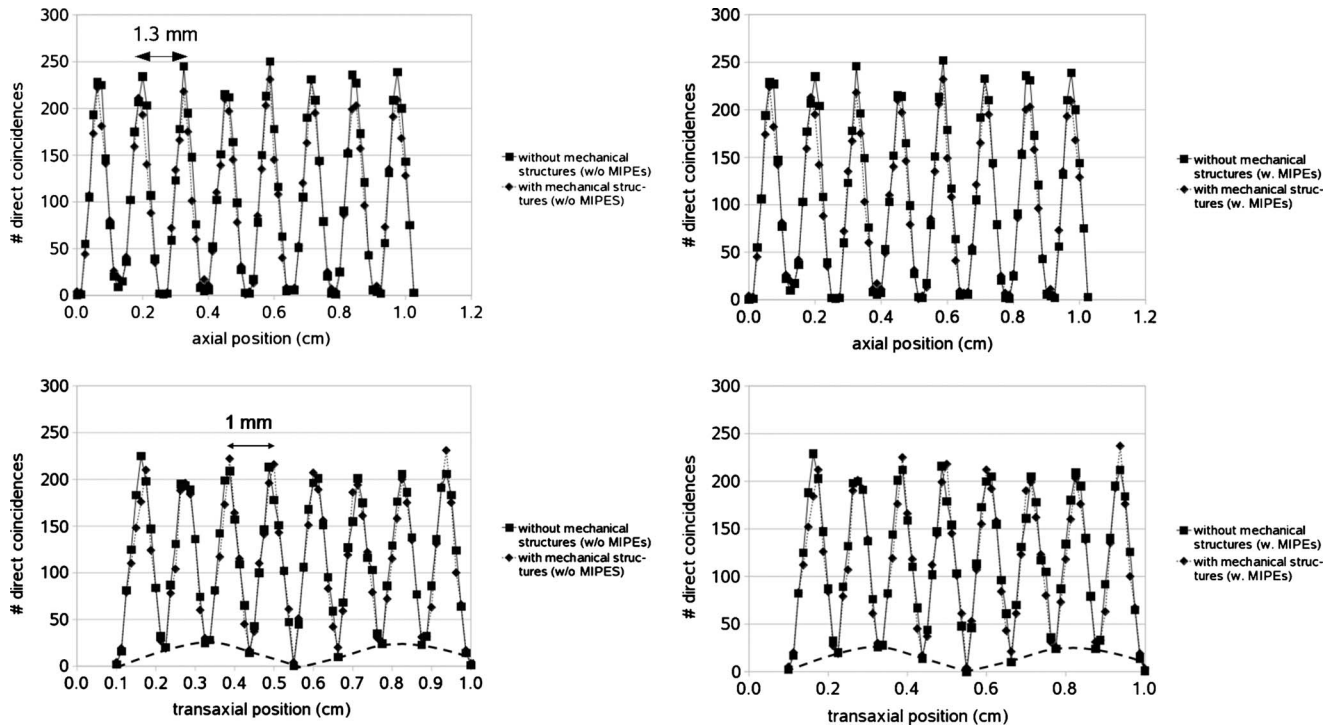


FIG. 14. Coincidence profiles as a function of source position when the coincidence photon beam is translated along the axial ( $z$  direction, top) and the transaxial ( $y$  direction, bottom) FoV. The dashed curves in the transaxial profiles indicate an enhanced background pattern due to position binning errors in the  $y$  direction.

### III.B.2. Reconstructed spatial resolution

Four point sources of 1 mm diameter each, placed at different radial offsets in the FoV (0, 0.5, 1, and 1.5 cm) within a cold water background, were simulated and reconstructed using an iterative 3D list-mode OSEM algorithm. List-mode statistical iterative image reconstruction was preferred against filtered backprojection since it more accurately treats the irregular dual-panel system geometry, which has only limited angular sampling. The algorithm uses two iterations and ten subsets. The images were reconstructed using a pixel size of 250  $\mu\text{m}$  and with the options of either including or excluding MIPES within an energy window of 450–700 keV. Figure 15 shows the reconstructed image slices taken through the spheres and parallel to the panels. All the images were scaled with respect to the reconstructed image in case of no interspersed mechanical structures present and MIPES included (top left image in Fig. 15). In the case of MIPES included in the analysis, a moderate background is visible between the sources as a result of event mispositioning due to the energy weighted mean algorithm. The background is less visible at large radial offsets owing to the reduced system sensitivity away from the center of the FoV.

The dependence of the reconstructed spatial resolution on radial offset is shown in Fig. 16. The spatial resolution values are calculated from the position profiles along a central slice (Fig. 15) and were averaged over the transaxial and sagittal views with associated error values (of the average) also shown in Fig. 16. The dependence is plotted for the cases with and without mechanical structures and with and without MIPES. Table IV summarizes the spatial resolution nonuniformity (defined as  $[(\text{FWHM}_{1.5 \text{ cm}} - \text{FWHM}_{0 \text{ cm}})/\text{FWHM}_{0 \text{ cm}}] \times 100\%$ , with  $\text{FWHM}_{1.5 \text{ cm}}$  and  $\text{FWHM}_{0 \text{ cm}}$  being the calculated FWHM of the position profiles at radial offsets of 1.5 and 0 cm, respectively) for each of the aforementioned cases.

## IV. DISCUSSION

A comparison of the LYSO energy spectra in the absence and presence of the mechanical structures in Fig. 6 shows that the presence of the interspersed mechanical structures (shown in Figs. 2 and 3) results in a reduction in the recorded singles events in the 511 keV photopeak. The figure also shows an enhancement of the recorded photon flux resulting

TABLE II. The calculated crystal pitch values based on the profiles of Fig. 14.

Crystal pitch	Without mechanical structures interspersed (mm)	With mechanical structures interspersed (mm)
Axial (along $z$ )	$(1.304 \pm 0.067)$	$(1.304 \pm 0.067)$
Transaxial (along $y$ )	$(1.107 \pm 0.086)$	$(1.089 \pm 0.061)$

TABLE III. The calculated intrinsic spatial resolution values based on the profiles of Fig. 14.

Profile FWHM	Without mechanical structures interspersed (mm)	With mechanical structures interspersed (mm)
Axial (along $z$ )	$(0.55 \pm 0.05)$	$(0.56 \pm 0.02)$
Transaxial (along $y$ )	$(0.62 \pm 0.03)$	$(0.59 \pm 0.04)$

from incident photons that have been backscattered in the Al mechanical structures and subsequently deposit their residual energy of approximately 170 keV in the crystal. This is confirmed by the observed peak at an energy of approximately 340 keV on the spectrum of the deposited energy in the mechanical structures seen at the bottom plot in Fig. 6 (black dashed line).

From the profiles of Fig. 7, it is evident that changes in photon detection efficiency are predominantly dependent on the volume of the mechanical structures as well as their position with respect to the incident radiation. In the case of a point source placed at the center of the FoV for the front and the middle sections of the mechanical structure (the distinction between front, middle, and rear sections is shown in Fig. 5), a comparable number of total photon interactions is observed with slight enhancement in the case of the middle section, as illustrated quantitatively in Fig. 8.

The above observation is attributed to the fact that the middle section has a larger volume (almost twice the volume of the front section, see Fig. 2) and will also encounter a higher number of scattered (less energetic) photons, thus the probability for further attenuation is enhanced. It should also be mentioned that the source is not collimated, thus contributing buildup events, that is, events detected due to scatter in surrounding material, to the middle and rear sections; however, the general exponential attenuation of the incident radiation is observed especially along the significantly larger length of the rear section, as well as following the envelope of the counts shown in each section (Fig. 7). Contrarily, in the case of a uniform source placed at the center of the FoV, the trend observed between the front and the middle sections is somewhat reversed, given the fact that a large portion of the photon flux incident on the front section of the mechani-

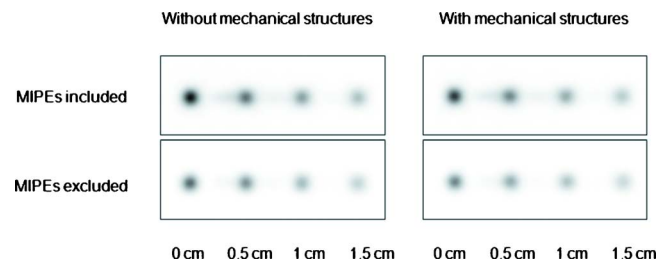


FIG. 15. 3D list-mode OSEM reconstructed images (two iterations and ten subsets) of four 1 mm diameter point sources in water without (left) and with (right) the interspersed mechanical structures with (top) and without (bottom) MIPEs included in the analysis (positioned with energy weighted mean over all interactions). A central slice parallel to the  $x$ - $y$  plane is shown. The sources are placed at radial offsets of 0, 0.5, 1, and 1.5 cm from the center of the FoV. All images are scaled with respect to the top left one.

cal structures is already less energetic (compared to the case of a point source) having a higher chance of already interacting with the source material itself. This is also confirmed by the energy spectra of Fig. 9 where it is shown that the front section encounters a higher number of low energy depositions in the case of the uniform source and compared to the other two sections.

From the  $z$  profile, the contribution of the different materials of the mechanical structure ( $\text{Al}_2\text{O}_3 + \text{Al}$ ) is indicated by the highlighted regions for one detector layer and it does not exhibit noticeable variations per unit length among the different components in each layer.

The histograms of Fig. 9 indicate that the preferred energy range of the absorbed photons has a slight dependence on the position of the mechanical structures and on the configuration of the radiation source. The negative local minimum observed in both plots of Fig. 10 for a lower energy threshold of 100 keV is directly related to the increase in the registered photon flux (approximately 14% and 7% for singles at a 100–200 keV energy window and coincidences above 100 keV, respectively) resulting from the presence of the mechanical structures, as illustrated in Fig. 6 and explained in the beginning of this section.

Concerning MIPEs, the simulation results show that the probability that multiple interactions occur within the same coincidence time window follows an exponential decrease with the interaction number, as illustrated in Fig. 13. However, the effect of the interspersed mechanical structures on

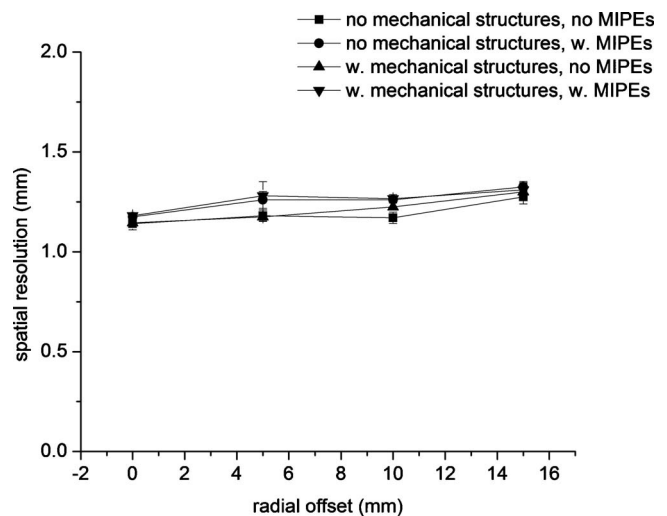


FIG. 16. Spatial resolution as a function of radial offset calculated from the radial profiles of the reconstructed point sources along a central slice parallel to the  $x$ - $y$  plane (see Fig. 5 for the axis definition).

TABLE IV. The calculated reconstructed spatial resolution nonuniformity based on the plot of Fig. 16.

Resolution nonuniformity	Without mechanical structures interspersed (%)	With mechanical structures interspersed (%)
Including MIPes	13	11
Excluding MIPes	12	13

the sensitivity of MIPes increases with increasing number of interactions involved in a MIPe for the point source geometry, as evidenced from the data of Table I. No consistent trend is observed for the slab source geometry in the case that the total number of interactions within the same coincidence time window is larger than 4. These differences may be attributed to the different intensity and angular distributions of the incident photon flux that every detector encounters for each of the two different source geometries, as well as the different energies of the incident photons; in the case of a point source the incident energy is 511 keV, whereas for the uniform source photon scatter in the source material results in energetically lower incident photons. Even though the current analysis considers only MIPes occurring between different detector arrays, while it processes MIPes occurring within the same array as a single event (with energy equal to the energy sum of the individual interactions), it is not expected that mechanical structures will have a considerable effect on the latter given the fact that the only material interspersed between the crystal elements is the reflector sheet.

The FWHM of the axial and transaxial profiles shown in Fig. 14 and summarized in Table III did not show significant degradation between the two cases (with and without mechanical structures present). The enhanced background pattern observed in the case of the transaxial position profile (dashed curves in Fig. 14) is attributed to systematic uncertainties introduced by the estimation of the center position of every crystal pixel in the  $y$  direction during the virtual segmentation of the simulated crystal slab into an  $8 \times 8$  crystal array (and the corresponding rebinning of the simulated events into the  $1 \text{ mm}^3$  crystal bins). This background pattern is not observed in the axial profile data given the fact that the axial crystal sheets are modeled as in reality, that is, no event rebinning is performed in the  $z$  direction.

The data in Fig. 16 and in Table IV indicate that there is no considerable effect of the mechanical structures or including MIPes on the reconstructed spatial resolution and spatial resolution uniformity. However, Fig. 15 indicates that the aforementioned sensitivity degradation with the mechanical structures present is more prominent for MIPes and is clearly reflected in the reconstructed images.

## V. CONCLUSION

This study investigates the effect of interspersed mechanical structures within a dual-panel, breast-dedicated PET system design comprising densely packed scintillation detectors in terms of the photon sensitivity and spatial resolution. The results of this study have a broader applicability to various

PET system designs given the increased need for reliable and reproducible system performance. To date, there are a large number of high resolution designs that employ structures in the vicinity of the detectors (such as additional detector material, substrates, PCBs, chassis etc.) that may potentially impair performance parameters, such as sensitivity and spatial resolution. One example is a detector with alternative DoI designs, such as dual-ended crystal readout with avalanche photodiodes (APDs) (Ref. 26) where one of the two photodetectors is placed right in front of the crystal face. Another example is a high resolution PET imager employing silicon scatter detectors<sup>27</sup> in which an inner detector ring (insert) is placed within the FoV of a conventional PET ring. We claim that the results presented in this study prove the importance of studying the aforementioned effects in any such system.

The design under study consists of several thin Al and  $\text{Al}_2\text{O}_3$  mechanical structures interspersed between the LYSO-PSAPD detector arrays for mechanical support and in order to achieve crystal positioning accuracy and detector temperature stability. The presented analysis showed that the mechanical structures have a larger effect on the multi-interaction photon events, namely, photons that have undergone multiple interactions among several detector units, compared to coincident events involving only a single interaction in each panel. The mechanical structures act as an attenuation medium for all types of photon interactions, resulting in mean degradations of 6.5% and 12.5% on the single photon and the coincidence photon detection efficiency, respectively, for a 450–700 keV energy window. In addition, it was shown that in the case of MIPes, this degradation is more prominent with increasing number of interactions per incident photon. In the case of a point source geometry, this effect is evident for every number of MIPes considered in this study. However, in the case of a uniform source geometry, the effect is evident only for a number of MIPes below 4. Despite the detection efficiency degradation, the effect on both intrinsic and reconstructed spatial resolution was estimated to be minor, thus enhancing the hypothesis that MIPes may have an effect on the image contrast but not necessarily on the spatial resolution.

Proper identification and consideration of multi-interaction photon events, especially in systems employing small detector elements in order to improve spatial resolution, is currently an active field of research.<sup>19–21</sup> Sophisticated algorithms are currently under development in order to accurately identify, position, and include these events in the analysis.<sup>19–21</sup> If successful, the accurate identification of such

events will greatly enhance the system's sensitivity while maintaining or even improving the achieved spatial resolution.<sup>25</sup> Thus, in systems where the multi-interaction photon events account for the majority of the recorded coincidences, such as the system under study, identification and eventually inclusion of MIPEs may result in an overall increase in system sensitivity. However, if the actual number of detected MIPEs is reduced due to the interspersed mechanical structures between the detector arrays (reaching up to 20% reduction in the system under study), the net increase in the overall system sensitivity (due to the inclusion of MIPEs in the analysis) may become less beneficial than initially predicted. Currently interspersed Al<sub>2</sub>O<sub>3</sub> as well as Al structures that will assure a good compromise between mechanical robustness, temperature stability, and satisfactory system performance are under evaluation.

In addition to the mechanical structures investigated in this study, the sides of the scanner head under construction will be appropriately shielded against radiation from outside the field of view, especially from organs of high radiotracer uptake adjacent or relatively near to the breast, such as the heart, the liver, and the brain. We do not expect an effect of the outer shielding on the quoted results, which are specific to the scatter environment under the influence of the mechanical structures interspersed between the 8 × 8 detector arrays. Future work will focus on designing and developing this external shielding as well as on investigating the effect of the shielding and complete panel assembly (Fig. 4) on the scanner's performance parameters.

## ACKNOWLEDGMENTS

The authors would like to thank C. Fang and J. Zhai for their contribution in designing and manufacturing the mechanical structures studied in this work. The help of Dr. G. Chinn with the use of the OSEM reconstruction algorithm and of P. Olcott and Y. Gu for providing input on using the GRAY simulation software is greatly acknowledged. This work was supported by the NIH under Grant Nos. R01 CA119056, R01 CA119056-S1 (ARRA), and R33 EB003283, the AXA Research Fund, the Bio-X Graduate Student Fellowship, the Belgian-American Research Foundation and Grant No. DOD BC094158.

<sup>a)</sup>Electronic mail: cslevin@stanford.edu

<sup>1</sup>A. Karellas and S. Vedantham, "Breast cancer imaging: A perspective for the next decade," *Med. Phys.* **35**, 4878–4897 (2008).

<sup>2</sup>M. K. O'Connor and G. Tourassi, "Molecular breast imaging will soon replace x-ray mammography as the imaging modality of choice for women at high risk with dense breasts," *Med. Phys.* **36**, 1463–1466 (2009).

<sup>3</sup>L. M. Peterson *et al.*, "Quantitative imaging of estrogen receptor expression in breast cancer with PET and <sup>18</sup>F-fluoroestradiol," *J. Nucl. Med.* **49**, 367–374 (2008).

<sup>4</sup>N. Avril *et al.*, "Glucose metabolism of breast cancer assessed by <sup>18</sup>F-FDG PET: Histologic and immunohistochemical tissue analysis," *J. Nucl. Med.* **42**, 9–16 (2001).

<sup>5</sup>N. K. Doshi *et al.*, "Design and evaluation of an LSO PET detector for breast cancer imaging," *Med. Phys.* **27**, 1535–1543 (2000).

<sup>6</sup>F. Lamare *et al.*, "Design simulation of a rotating dual-headed PET/CT scanner for breast imaging," *IEEE NSS/MIC Conference Record*, pp. 1740–1744, 2005.

<sup>7</sup>Y. Wu *et al.*, "Characteristics of the PET component of a dedicated breast PET/CT scanner prototype," *IEEE NSS/MIC Conference Record*, pp. 2335–2339, 2006.

<sup>8</sup>S. Surti and J. S. Karp, "Design considerations for a limited-angle, dedicated breast TOF PET scanner," *Phys. Med. Biol.* **53**, 2911–2921 (2008).

<sup>9</sup>R. R. Raylman *et al.*, "The positron emission mammography/tomography breast imaging and biopsy system (PEM/PET): Design, construction and phantom-based measurements," *Phys. Med. Biol.* **53**, 637–653 (2008).

<sup>10</sup>S. L. Bowen *et al.*, "Initial characterization of a dedicated breast PET/CT scanner during human imaging," *J. Nucl. Med.* **50**, 1401–1408 (2009).

<sup>11</sup>D. B. Keesing *et al.*, "System modeling of a DOI-capable half-ring PET insert device for breast cancer imaging," *IEEE NSS/MIC Conference Record*, pp. 4218–4222, 2008.

<sup>12</sup>J. Zhang *et al.*, "Study of the performance of a novel 1 mm resolution dual-panel PET camera design dedicated to breast cancer imaging using Monte Carlo simulation," *Med. Phys.* **34**, 689–702 (2007).

<sup>13</sup>J. Zhang *et al.*, "Performance characterization of a novel thin position-sensitive avalanche photodiode for 1 mm resolution positron emission tomography," *IEEE Trans. Nucl. Sci.* **54**, 415–421 (2007).

<sup>14</sup>C. S. Levin, "Design of a high-sensitivity scintillation crystal array for PET with nearly complete light collection," *IEEE Trans. Nucl. Sci.* **49**, 2236–2243 (2002).

<sup>15</sup>P. A. Dokhale *et al.*, "Performance measurements of a depth-encoding PET detector module based on position-sensitive avalanche photodiode read-out," *Phys. Med. Biol.* **49**, 4293–4304 (2004).

<sup>16</sup>C. W. Lerche *et al.*, "Depth of  $\gamma$ -ray interaction within continuous crystals from the width of its scintillation light-distribution," *IEEE Trans. Nucl. Sci.* **52**, 560–572 (2005).

<sup>17</sup>V. Ch. Spanoudaki *et al.*, "Effect of temperature on the performance of proportional APD-based modules for gamma-ray detection in positron emission tomography," *IEEE Trans. Nucl. Sci.* **55**, 469–480 (2008).

<sup>18</sup>G. Pratz *et al.*, "Accurately positioning events in a high resolution PET system that uses 3D CZT detectors," *IEEE NSS/MIC Conference Record*, pp. 2660–2664, 2007.

<sup>19</sup>G. Pratz *et al.*, "Bayesian reconstruction of photon interaction sequences for high-resolution PET detectors," *Phys. Med. Biol.* **54**, 5073–5094 (2009).

<sup>20</sup>M. Rafecas *et al.*, "Inter-crystal scatter in a dual layer, high resolution LSO-APD positron emission tomograph," *Phys. Med. Biol.* **48**, 821–848 (2003).

<sup>21</sup>I. Torres-Espallardo *et al.*, "Effect of inter-crystal scatter on estimation methods for random coincidences and subsequent correction," *Phys. Med. Biol.* **53**, 2391–2411 (2008).

<sup>22</sup>F. W. Y. Lau *et al.*, "1 mm<sup>3</sup> resolution breast-dedicated PET system," *IEEE NSS/MIC Conference Record*, pp. 5619–5622, 2008.

<sup>23</sup>P. D. Olcott *et al.*, "GRAY: High energy photon ray tracer for PET applications," *IEEE NSS/MIC Conference Record*, pp. 2011–2015, 2006.

<sup>24</sup>A. Vandenbroucke, A. M. K. Foudray, P. D. Olcott, and C. S. Levin, "Performance characterization of a new high resolution PET scintillation detector," *Phys. Med. Biol.* **55**, 5895–5911 (2010).

<sup>25</sup>Y. Gu, G. Pratz, F. W. Y. Lau, and C. S. Levin, "Effects of multiple-interaction photon events in a high-resolution PET system that uses 3-D positioning detectors," *Med. Phys.* **37**, 5494–5508 (2010).

<sup>26</sup>Y. Yang *et al.*, "A prototype PET scanner with DOI-encoding detectors," *J. Nucl. Med.* **49**, 1132–1140 (2008).

<sup>27</sup>S.-J. Park *et al.*, "Performance evaluation of a very high resolution small animal PET imager using silicon scatter detectors," *Phys. Med. Biol.* **52**, 2807–2826 (2007).